

# Northumbria Research Link

Citation: Huang, Ziyi, Liu, Dejun, Wu, Qiang, Tian, Ke, Zhao, Haoyu, Shen, Changyu, Farrell, Gerald, Semenova, Yuliya and Wang, Pengfei (2022) Light transmission mechanisms in a SMF-capillary fiber-SMF structure and its application to bi-directional liquid level measurement. *Optics Express*, 30 (12). pp. 21876-21893. ISSN 1094-4087

Published by: Optical Society of America

URL: <https://doi.org/10.1364/OE.456917> <<https://doi.org/10.1364/OE.456917>>

This version was downloaded from Northumbria Research Link:  
<http://nrl.northumbria.ac.uk/id/eprint/49636/>

Northumbria University has developed Northumbria Research Link (NRL) to enable users to access the University's research output. Copyright © and moral rights for items on NRL are retained by the individual author(s) and/or other copyright owners. Single copies of full items can be reproduced, displayed or performed, and given to third parties in any format or medium for personal research or study, educational, or not-for-profit purposes without prior permission or charge, provided the authors, title and full bibliographic details are given, as well as a hyperlink and/or URL to the original metadata page. The content must not be changed in any way. Full items must not be sold commercially in any format or medium without formal permission of the copyright holder. The full policy is available online: <http://nrl.northumbria.ac.uk/policies.html>

This document may differ from the final, published version of the research and has been made available online in accordance with publisher policies. To read and/or cite from the published version of the research, please visit the publisher's website (a subscription may be required.)








**Northumbria  
University**  
NEWCASTLE



**UniversityLibrary**



# Light transmission mechanisms in a SMF-capillary fiber-SMF structure and its application to bi-directional liquid level measurement

ZIYI HUANG,<sup>1</sup> DEJUN LIU,<sup>1,2,9</sup>  QIANG WU,<sup>3,4</sup>  KE TIAN,<sup>5</sup>   
HAOYU ZHAO,<sup>6</sup> CHANGYU SHEN,<sup>7</sup>  GERALD FARRELL,<sup>8</sup>  YULIYA SEMENOVA,<sup>8</sup> AND PENGFEI WANG<sup>1,5,10</sup>

<sup>1</sup>Key Laboratory of Optoelectronic Devices and Systems of Ministry of Education and Guangdong Province, College of Physics and Optoelectronic Engineering, Shenzhen University, Shenzhen, 518060, China

<sup>2</sup>Shenzhen Key Laboratory of Photonic Devices and Sensing Systems for Internet of Things, Guangdong and Hong Kong Joint Research Centre for Optical Fibre Sensors, Shenzhen University, Shenzhen, 518060, China

<sup>3</sup>Key Laboratory of Nondestructive Test (Ministry of Education), Nanchang Hangkong University, Nanchang, 330063, China

<sup>4</sup>Department of Mathematics, Physics and Electrical Engineering, Northumbria University, Newcastle Upon Tyne, NE1 8ST, United Kingdom

<sup>5</sup>Key Lab of In-Fiber Integrated Optics, Ministry Education of China, Harbin Engineering University, Harbin, 150001, China

<sup>6</sup>Technical Center, Sichuan Changhong Electric Co., Ltd, Mianyang, 621000, China

<sup>7</sup>Institute of Optoelectronic Technology, China Jiliang University, Hangzhou, 310018, China

<sup>8</sup>Photonics Research Centre, Technological University Dublin, Grangegorman Campus, Dublin, Ireland

<sup>9</sup>dejun.liu@szu.edu.cn

<sup>10</sup>pfwang@szu.edu.cn

**Abstract:** Capillary fiber (CF) has been extensively investigated in a singlemode fiber (SMF)-CF-SMF (SCS) sensing structure since multiple light guiding mechanisms can be easily excited by simply tuning the air core diameter (cladding diameter) and length of the CF. Understanding the light guiding principles in an SCS structure is essential for improved implementation of a CF based fiber sensor. In this work, light guiding principles in a relatively large air core diameter ( $\geq 20 \mu\text{m}$ ) and long length of CF ( $> 1 \text{ mm}$ ) are investigated theoretically and experimentally. It is found that both multimode interference (MMI) and Anti-Resonant Reflecting Optical Waveguide (ARROW) light guiding mechanisms are excited in the SCS structure in the transmission configuration. However, MMI dips are not observed in the spectrum for the air core diameters of CF smaller than  $50 \mu\text{m}$  in the experiment due to large transmission loss in small air core CFs. Further experimental results demonstrate that a CF with a bigger air core diameter shows a higher sensitivity to curvature, and the highest sensitivity of  $-16.15 \text{ nm/m}^{-1}$  is achieved when an CF-100 was used. In addition, a SMF-CF-20-CF-30-SMF (SCCS) structure is proposed for high sensitivity bi-direction liquid level measurement for the first time, to the best of our knowledge. Two types of ARROW dips (Dip-20 and Dip-30) are simultaneously excited in transmission, hence both liquid level and liquid flow direction can be detected by tracing the dip strength changes of Dip-20 and Dip-30, respectively.

© 2022 Optica Publishing Group under the terms of the [Optica Open Access Publishing Agreement](#)

## 1. Introduction

For over a decade, anti-resonant hollow core fibers (ARHCFs) have been extensively investigated for use in a diverse range of areas, including ultrafast optics, low loss optical communications and

sensing applications due to their low dispersion, low nonlinear response, high damage threshold and the ease with which the air hole can be infiltrated with gases and liquids for an enhanced interaction between light and matter [1–4]. To date, many different types of ARHCFs have been proposed, such as a hollow core photonic crystal fiber (HCPCF) [5–7], a hole-assisted dual-core fiber [8–9], a single hole twin eccentric cores fiber [10–11], a negative curvature hollow core fiber [12] and a capillary fiber (CF) [13–24]. Among those ARHCFs, CF has attracted considerable interest when used in a singlemode fiber (SMF)-CF-SMF (SCS) structure for sensing applications due to its simple configuration and easy fabrication process. There have been many reports in the literature of the use of such SCS structures to measure a wide variety of environmental parameters including temperature [14–16], humidity [17], curvature [18–19], twist [20–21], strain [22], liquid level [23–24] and so on.

Recently combining different light guiding mechanisms (for example, Fabry-Perot interference (FPI), Mach-Zehnder interference (MZI), Multimode interference (MMI) and Anti-Resonant Reflecting Optical Waveguide (ARROW) guiding mechanism) in a fiber sensor structure has been shown to be a useful means to implement simultaneous monitoring of multiple parameters. Combining different light guiding mechanisms in a single SCS structure can be achieved by deliberate selection of specific values of the diameter of the air core, the fusion splicing power and the CF length [18,25–28]. For example, Gao *et al.* reported and experimentally demonstrated an SCS structure for high sensitivity pressure sensing with self-temperature calibration with hundreds of micrometers length of a CF, where both ARROW and FPI light guiding mechanisms were excited in its reflection spectrum [25]. Wang *et al.* proposed a SCS structure based on a large air core diameter (50  $\mu\text{m}$ ) CF which combined ARROW and MZI guiding mechanisms to realize a high sensitivity curvature sensor with low temperature cross-sensitivity by tracking the wavelength interval between dips resulted from the two mechanisms [18]. Cheng *et al.* introduced two up-tapers at the connection points between the CF and SMFs to excite both MZI and ARROW mechanisms for simultaneous measurement of curvature and temperature [26]. Finally Nan *et al.* reported a SMF-air bubble-CF-up taper-SMF hybrid structure which combined FPI, MZI and ARROW mechanisms for measurement of curvature, temperature and transverse load [27].

To design an improved CF based fiber sensor structure, which offers for example a higher sensitivity and/or lower cross sensitivities and/or multiple parameters measurement, it is essential to understand the light guiding principles in a SCS structure. Sun *et al.* have reported a comparative study on light transmission mechanisms in an SCS structure with different CFs, which demonstrates that the emergence of one or hybrid light transmission mechanisms (MMI, FPI, MZI and ARROW) is determined by both the inner diameter and length of the CF [28]. Yu *et al.* have also theoretically and experimentally demonstrated the coexistence of FPI, MZI and ARROW guiding mechanisms in a simple SCS cascaded structure, which was used to independently measurement of multiple parameters including temperature and strain [29]. However whilst in the works mentioned above the CF used had a relatively small air core diameter ( $\leq 20 \mu\text{m}$ ) and a short length ( $< 1 \text{ mm}$ ), CF with a larger air core diameter and longer length are more frequently used in practice to achieve a low transmission loss, easier infiltration of the air hole with gases and liquids if required and enhanced interaction between light and matter. However the transmission properties of such SCS structures have not yet been adequately investigated.

In this paper, a comprehensive theoretical and experimental study is reported on the light transmission mechanisms in an SCS structure with a wide range of CF air core diameters (20  $\mu\text{m}$ , 30  $\mu\text{m}$ , 50  $\mu\text{m}$  and 100  $\mu\text{m}$ ) and a much longer CF section length ( $> 1 \text{ mm}$ ). Both theoretical studies and experimental results have demonstrated that MMI and ARROW guiding mechanisms are excited in the proposed SCS structure in transmission. The SCS structure is further investigated as the basis of a sensor for curvature and liquid level measurement. It is

found that a CF with a larger air core diameter offers a much higher curvature sensitivity. The best curvature sensitivity of  $-16.15 \text{ nm/m}^{-1}$  was achieved when a CF-100 (core diameter of  $100 \mu\text{m}$ ) was used, which is much higher than that in many other reports [18,30–35]. In addition, a SMF-CF-30 (core diameter of  $30 \mu\text{m}$ )-CF-20 (core diameter of  $20 \mu\text{m}$ )-SMF (SCCS) structure is proposed for the first time for high sensitivity bi-direction liquid level measurement by tracking the changes in strength of the ARROW dips produced by CF-20 and CF-30, respectively.

## 2. Theoretical study

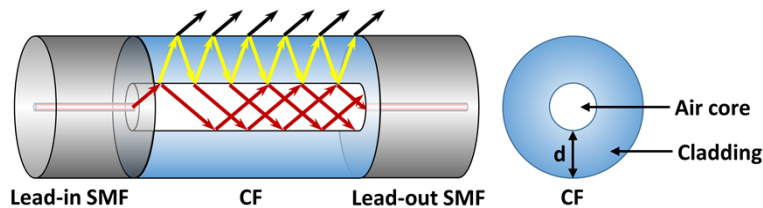
### 2.1. Light guiding principle of the SCS structure

Figure 1 illustrates the proposed SCS structure where a section of CF is sandwiched between two SMFs. The light guiding mechanism in an SCS structure is usually explained with a “ARROW” model (when a critical length of CF is satisfied [36]), in which the silica cladding can be viewed as a pair of FP etalons, where only certain wavelengths which meet the anti-resonance condition in the silica cladding, are confined and transmitted inside the air core, while other wavelengths which satisfy the resonance condition leak out into the surrounding environment and produce periodic dips in transmission spectrum. The resonant wavelengths and their free spectral range (FSR) can be calculated with the following equations [24]:

$$\lambda_m = \frac{2d\sqrt{n_1^2 - n_0^2}}{m} \quad (1)$$

$$FSR = \frac{\lambda_m \lambda_{m+1}}{2d\sqrt{n_1^2 - n_0^2}} \quad (2)$$

where  $d$  is the cladding thickness of the CF,  $n_0$  and  $n_1$  are the refractive indices of the air core and silica cladding of the CF, and  $m$  is the resonance order which is nonnegative integer. As can be seen from Eqs. (1) and (2), the resonant wavelengths and their FSRs are only dependent on the refractive index and thickness of the silica cladding, hence the resonant wavelengths can be set by selecting a CF with different air core diameters (assuming the diameter of the outer silica cladding is fixed). It is noted that an MZI is formed between core modes and cladding modes when the core diameter of an HCF and an SMF are comparable [24].



**Fig. 1.** The schematic diagrams of the SCS structure and a cross-section view of a CF.

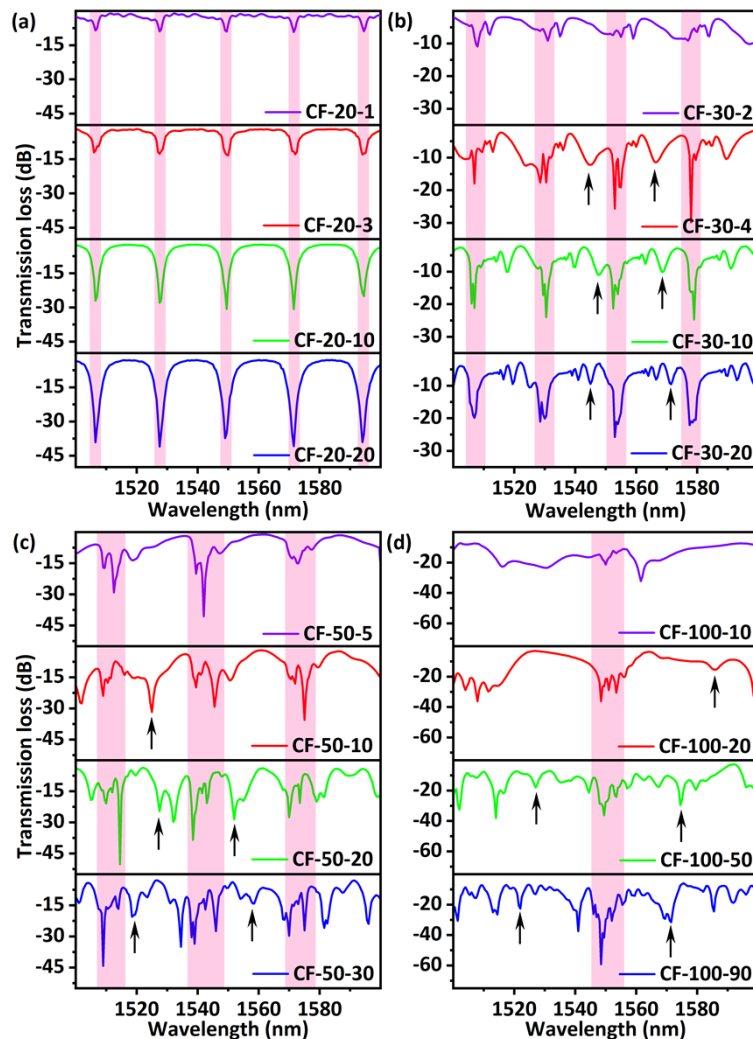
In this work, CFs with different air core diameters and lengths were used. The different CFs are denoted as CF-A-B, where A and B represent the air core diameter ( $\mu\text{m}$ ) and length (mm) of the CF, respectively. In the theoretical simulation, it was assumed that CFs are ideally fusion spliced with the SMFs without any collapse in the air core.

### 2.2. Simulation on light transmission properties of the SCS structure

First of all, the transmission properties of the proposed SCS structures with different air core

diameters and lengths of CF were theoretically investigated by using beam propagation method (BPM) where the refractive indices of the core and cladding of the CF are set to be 1 and 1.447.

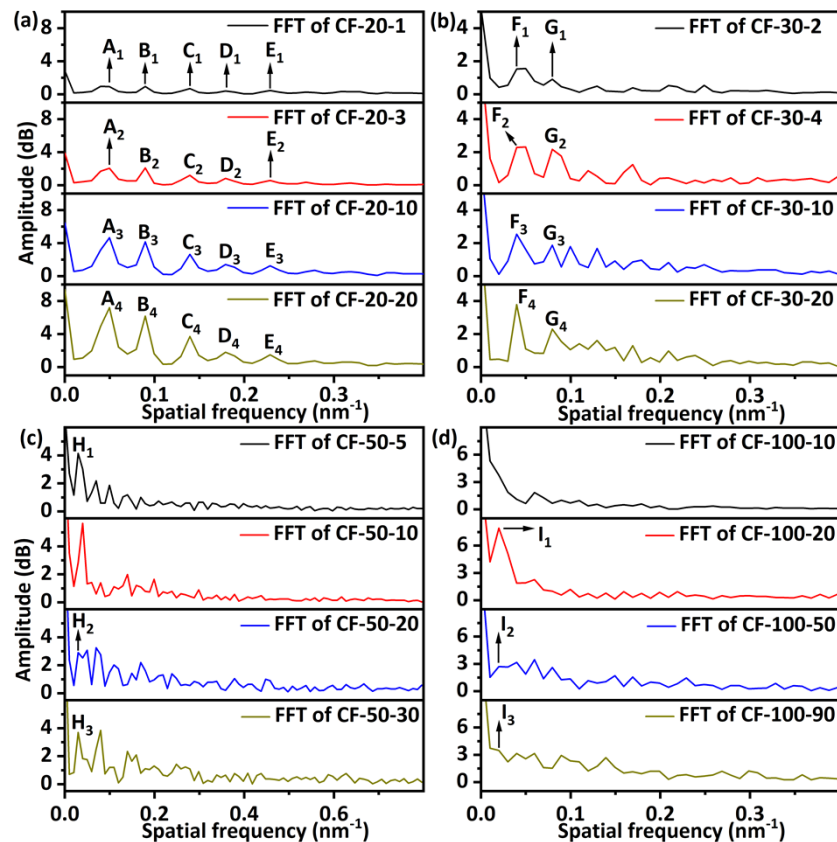
The simulated transmission spectra are displayed in Fig. 2. Periodic transmission dips with fixed central wavelengths and enhanced dip strength ( $\sim 2.5$  dB to  $\sim 40$  dB) are excited when the CF length is extended from 1 mm to 20 mm in a CF-20 as shown in Fig. 2 (a). The FSR between two adjacent transmission dips is 22.00 nm which agrees well with the theoretical value of 22.09 nm from Eq. (2). It is thus confirmed that those periodic dips are introduced by the ARROW guiding mechanism. When the air core diameter is increased to 30  $\mu\text{m}$  or larger, the FSR of the periodic transmission dips (highlighted with pink shade) increases as can be seen in Fig. 2 (b), (c) and (d). In addition, as the CF length increases a number of smaller dips appear in the transmission spectrum (as illustrated by arrows), whose central wavelengths change with the increase of the CF length. Considering that the air core diameter of the CF is much larger than the mode field diameter of the SMF, no cladding modes can be excited in the CF. Hence



**Fig. 2.** Simulated transmission spectra of a SCS structure with different air core diameters and lengths of the CF: (a) 20  $\mu\text{m}$ , (b) 30  $\mu\text{m}$ , (c) 50  $\mu\text{m}$  and (d) 100  $\mu\text{m}$ .

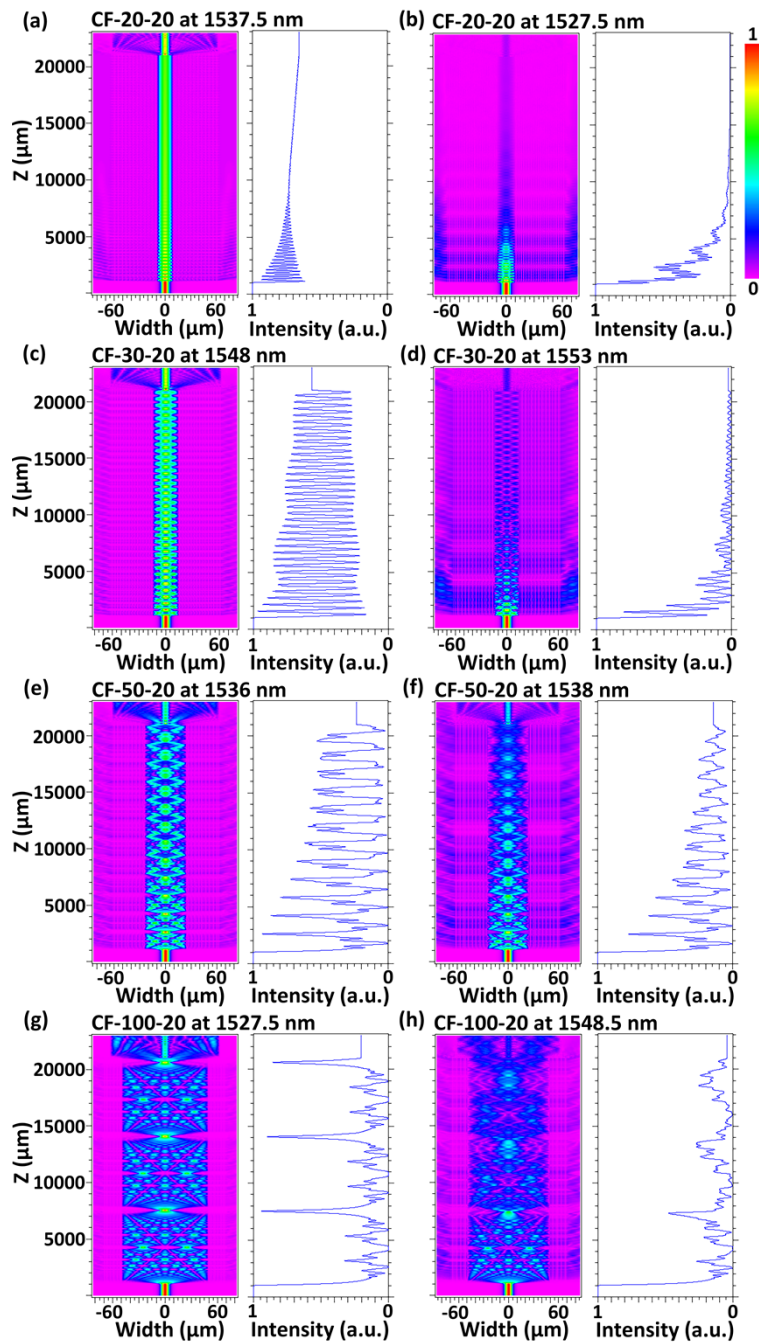
an MZI which relies on interference between core modes and cladding modes will not exist, as demonstrated recently for a CF-10 [24]. It can be concluded that these small dips are most likely excited by the MMI (between core modes). Some higher order modes could be excited at the fusion point between the SMF and CF due to the mismatch between mode field diameters. Multiple modes propagate along the CF and interfere with each other, which leads to MMI. It is noted that stronger ARROW dips are excited in a smaller air core diameter CF and in a longer length of CF since light experiences a greater number of reflections and hence produces stronger transmission dips, but with a higher overall transmission loss.

Figure 3 shows the frequency spectra of Fig. 2 analyzed with a fast Fourier transform (FFT) method. Five major frequencies (A, B, C, D, E) with fixed values are observed for all the different CF lengths in a CF-20 as shown in Fig. 3 (a), indicating excitation of multiple ARROW modes in CF-20 [28]. When the air core diameter is equal to 30  $\mu\text{m}$  or larger, some of the lower frequency peaks (corresponding to the lowest or the 2<sup>nd</sup> lowest frequencies) display no changes with the change of CF length, but other peaks, corresponding to higher frequencies are shifted, which indicates that another new guiding mechanism is excited.



**Fig. 3.** FFT spectra of the simulated transmission spectra of Fig. 2.

Figure 4. shows examples of the simulated energy distribution along the propagation distance ( $Z$ ) in CFs with different air core diameters but the same length (20  $\mu\text{m}$ ) at the anti-resonant and resonant wavelengths, respectively. In a CF-20-20, light transmission in the air core experiences a fast decline in power as a function of transmission distance at a resonant wavelength when light enters the CF-20 from an SMF. Comparing Fig. 4(a) and (b), the loss is smaller at an anti-resonant



**Fig. 4.** Simulated energy distributions for SCS structures with different core diameters of CF in the XZ plane: (a) CF-20-20, (c) CF-30-20, (e) CF-50-20, (g) CF-100-20 at anti-resonant wavelengths and (b) CF-20-20, (d) CF-30-20, (f) CF-50-20, (h) CF-100-20 at resonant wavelengths.

wavelength and the light intensity has a periodic behavior as a function of distance in the air core, with a period of 294.3  $\mu\text{m}$  with a gradually decreasing amplitude. The periodic behavior of the intensity results from interference between modes, their corresponding effective refractive indices (ERI) difference can be calculated when their phase difference ( $\phi = 2\pi\Delta n_{\text{eff}}L/\lambda$ ) is  $2\pi$  [37]. The calculated ERI difference is 0.00522 which is very small, hence interference is only happening between core modes.

It can also be seen from Fig. 4 that light propagation in a CF-20 experiences significant transmission loss with an increase in the length of the CF-20. Hence MMI dips are not found in a CF-20 as can be seen from Fig. 2 (a). With the increase in the length of the air core, more complex periodic behavior is evident and light transmission losses are significantly reduced at

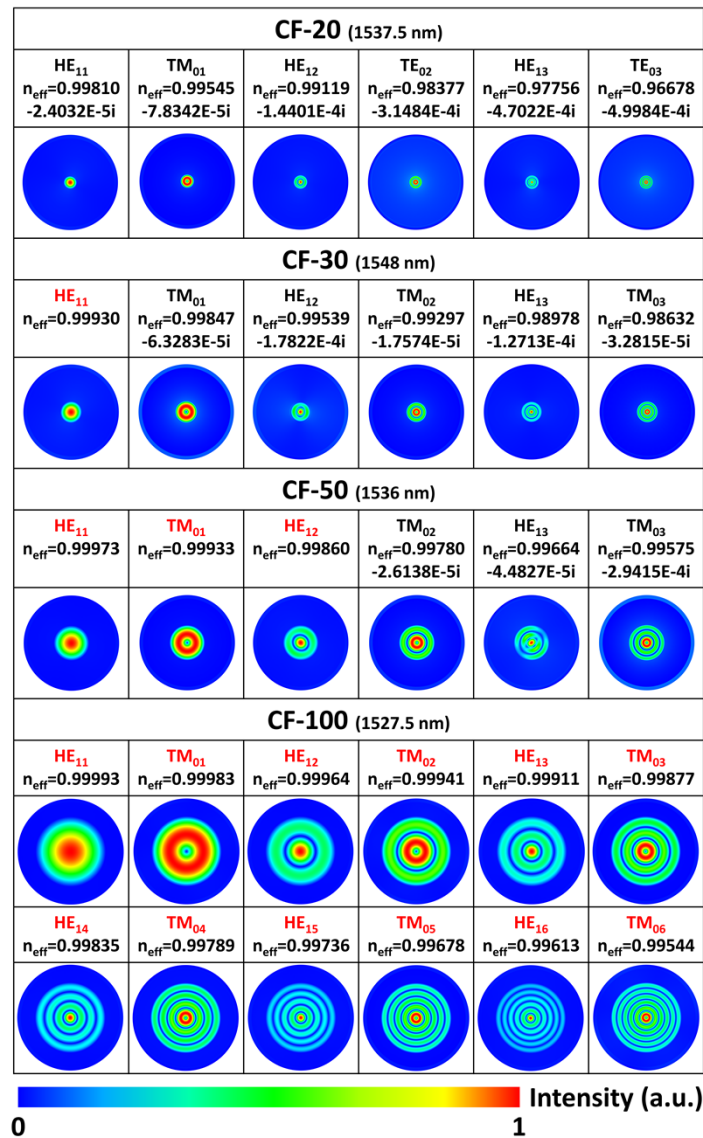


Fig. 5. Simulated mode field distributions in different types of CFs, including CF-20, CF-30, CF-50 and CF-100, with corresponding effective refractive indices.



both anti-resonant and resonant wavelengths. Self-imaging points could be clearly found in a CF-100-20 at an anti-resonant wavelength, which is clear evidence of MMI in the CF.

### 2.3. Simulation on mode field distributions in capillary fibers

For CFs with a larger air core diameter, more core modes will exist and hence increased mode interference will occur. To confirm the existence of multiple modes in CF with a larger core diameter and hence MMI, the mode field intensity distributions in the air core of a CF only were studied with a finite-element method (FEM) [31,38] and examples of the simulation results for several different CF core diameters are shown in Fig. 5. It can be seen that there is no guided mode in the CF-20 because even the fundamental mode has a complex value for the refractive index. High order leaky modes experience larger loss as can be seen from the increased value of the complex part of the RI. With the increase of the air core diameter of the CF, more guided modes are obtained, and hence lower transmission loss is achieved. In particular, one guided mode ( $HE_{11}$ ) is found in a CF-30, three are found in a CF-50, and over 12 guided modes are found in the CF-100. The ERI between  $HE_{12}$  and  $TM_{02}$  in a CF-100 is 0.00023 which is well matched with the calculated value (0.00023, calculated from the propagation distance period between the Self-imaging points) in Fig. 4 (g).

## 3. Experimental setup

In the experiment, four types of CFs with different air core diameters/cladding thicknesses were used (20  $\mu\text{m}$ / 53  $\mu\text{m}$ , 30  $\mu\text{m}$ / 48  $\mu\text{m}$ , 50  $\mu\text{m}$  / 38  $\mu\text{m}$  and 100  $\mu\text{m}$  / 20  $\mu\text{m}$ , Fiberguide Industries CAP020/150/24T, CAP030/150/24T, CAP050/150/24T and CAP100/164/24T). The SCS structure was fabricated by fusion splicing a short section of a CF between two SMFs using a Fujikura 62S+ fusion splicer (Fujikura (China) Co., Ltd.). The splicing parameters were carefully managed to avoid to the greatest extent possible collapse of the hollow core. An arc power of setting of -75 bit, and an arc time of 600 ms were used. Figure 6 (a) illustrates the experimental setup for recording the transmission spectra of the SCS structures. Figure 6 (b) shows several microscope images at the connection points between various CFs and SMFs. Light from a broadband supercontinuum source (SC, SC-YSL) was launched into the CF through an SMF, the output was detected by an optical spectrum analyzer (OSA). The sensors' responses to bending were also tested using this setup by simply moving the translation stages toward each other to realize different curvatures [39].

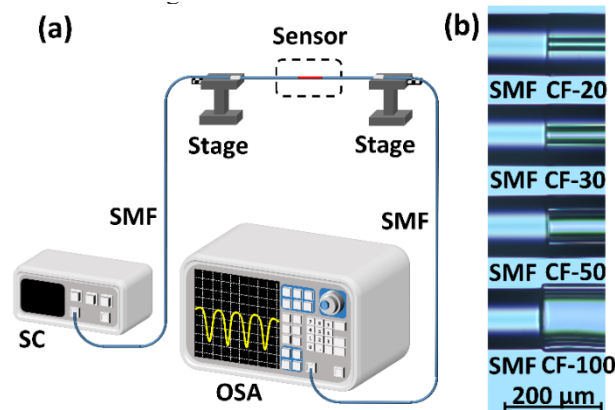
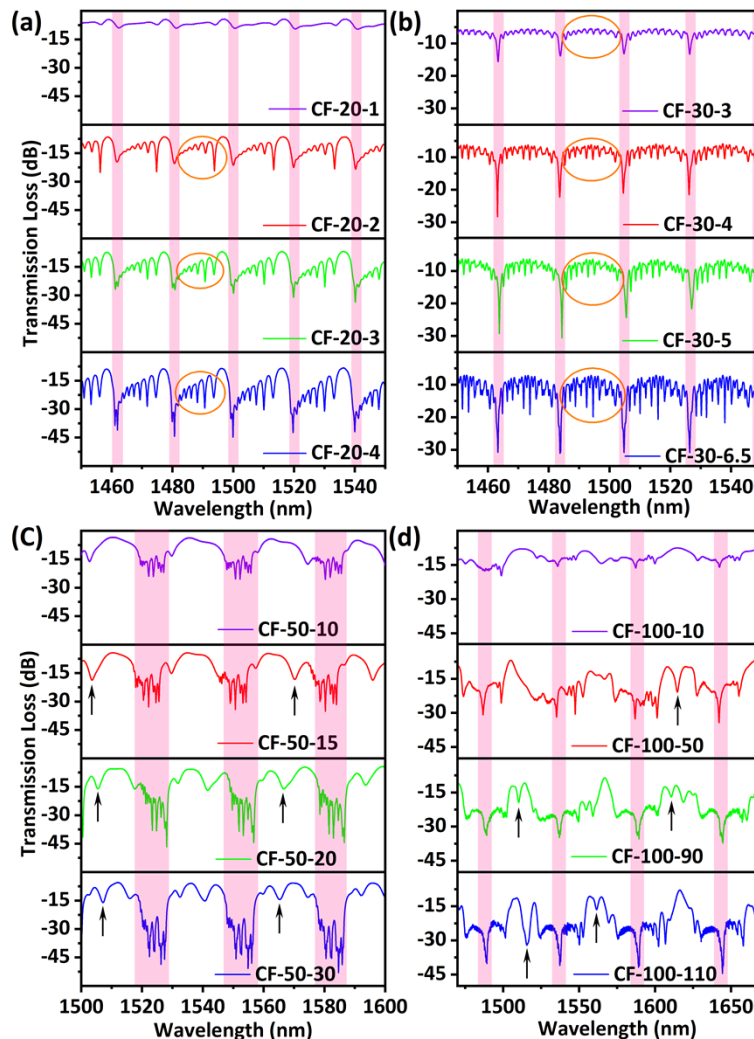


**Fig. 6.** (a) The schematic of the experimental setup for recording the transmission spectrum and for the curvature measurement and (b) Microscope images of the splicing joints of SMFs and CFs.

## 4. Results and discussion

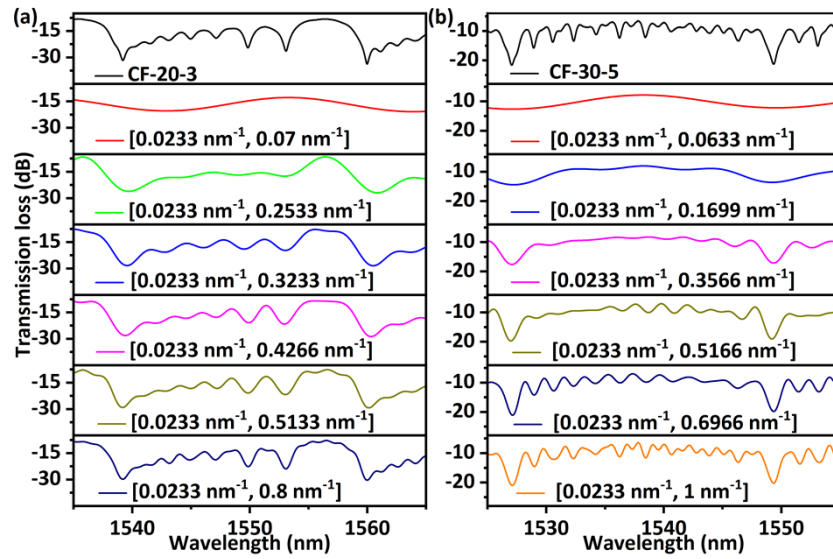
### 4.1. Experimental study on light transmission properties of the SCS structure

Figure 7 shows the experimentally measured transmission spectra of the proposed SCS structure with different air core diameters and lengths for the CF. As can be seen from Fig. 7 (a) and (b), a range of periodic strong transmission dips (pink shaded) are observed in CF-20 and CF-30 over the wavelength range from 1450 nm to 1550 nm and the central wavelengths of the dips are independent on the CF length. The FSRs of CF-20 and CF-30 are measured as 20.41 nm and 22.58 nm, which is well matched with the simulation results (22.00 nm and 24.00 nm) as shown in Fig. 2. As the air core diameter increases, ARROW dips could be still found with enlarged FSRs of 28.71 nm and 51.71 nm for a CF-50 and CF-100 as shown in Fig. 7 (c) and (d). In addition, some additional dips (marked by arrows) appear with varied central wavelengths and more dips are found in the structures with longer CFs, such as CF-50 and CF-100, which agrees with the simulation results. Those dips are most probably introduced by the MMI effect.



**Fig. 7.** Experimentally measured transmission spectra of a SCS structure with different air core diameters and lengths of CF: (a) 20  $\mu\text{m}$ , (b) 30  $\mu\text{m}$ , (c) 50  $\mu\text{m}$  and (d) 100  $\mu\text{m}$ .

In the experiment, in addition to the strong ARROW dips, some other small dips (marked with orange circles) are found in the spectra of CF-20 and CF-30 and they behave similarly to the strong ARROW dips. Many researchers attributed these small dips to possible non-uniformities of the ring cladding [40]. However, our results show that they are more likely introduced by other high order ARROW modes as can be seen from the decomposition of the transmission spectra with a band-pass filter method [10] as shown in Fig. 8, including decomposed spectra of CF-20-3 and CF-30-5.



**Fig. 8.** Decomposition of the transmission spectra of samples CF-20-3 and CF-30-5 using a band pass filter method.

Figure 9 shows the Fast Fourier Transform (FFT) frequency spectra of Fig. 7. It is found that the FFT spectra for CF-20 and CF-30 are similar as they both are independent on the CF length. They only differ in terms of the frequency peaks values, hence indicating the absence of the dips wavelengths shift in the transmission spectra. Unlike the simulation results shown in Fig. 2 and Fig. 3, fewer frequencies are found in Fig. 9 since in practice light guiding in a CF has a much higher loss due to the light absorption/scattering at the interface between CF cladding and air, which is not account for in the theoretical simulation. Hence MMI and the corresponding dips are not found in the transmission spectra of CF-30 as shown in Fig. 7 (b).

#### 4.2. Curvature sensing performance of the SCS structure

Since it was demonstrated that dips produced by MMI have high sensitivity to bending in terms of the central dip wavelength shift while ARROW dips show tiny wavelength shift with bending [18], a bending experiment was carried out to differentiate between the ARROW dips and MMI dips in the transmission spectra and to further confirm the existence of MMI in the SCS structure. Samples CF-20-3 mm, CF-30-4 mm, CF-50-30 mm and CF-100-110 mm were chosen for the bending experiment and the corresponding spectral responses are shown in Fig. 10. All the transmission dips of the CF-20 and CF-30 in Fig. 10 (a) and (b) experience very small wavelength shifts with changes in curvature. ARROW dips in the spectra of CF-50 and CF-100 (dip 50-B and dip 100-A) in Fig. 10 (c) and (d) show small changes in their central wavelengths, but other dips at anti-resonant wavelengths (dip 50-A and dip 100-B) show very significant wavelength shifts with curvature. It is thus possible to conclude that dip 50-A and dip 100-B are caused by

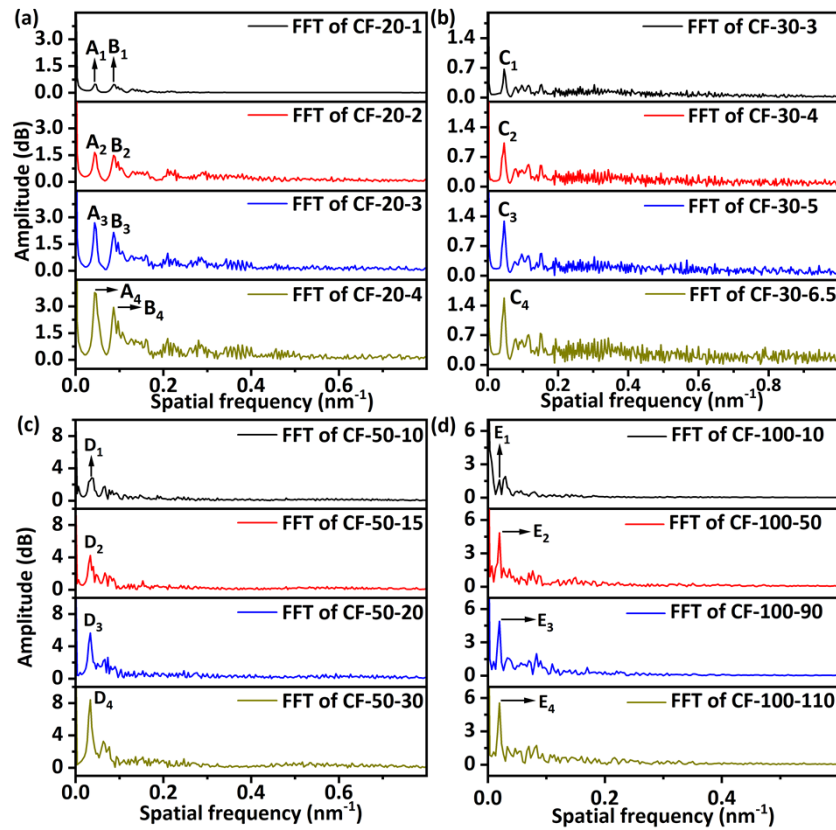
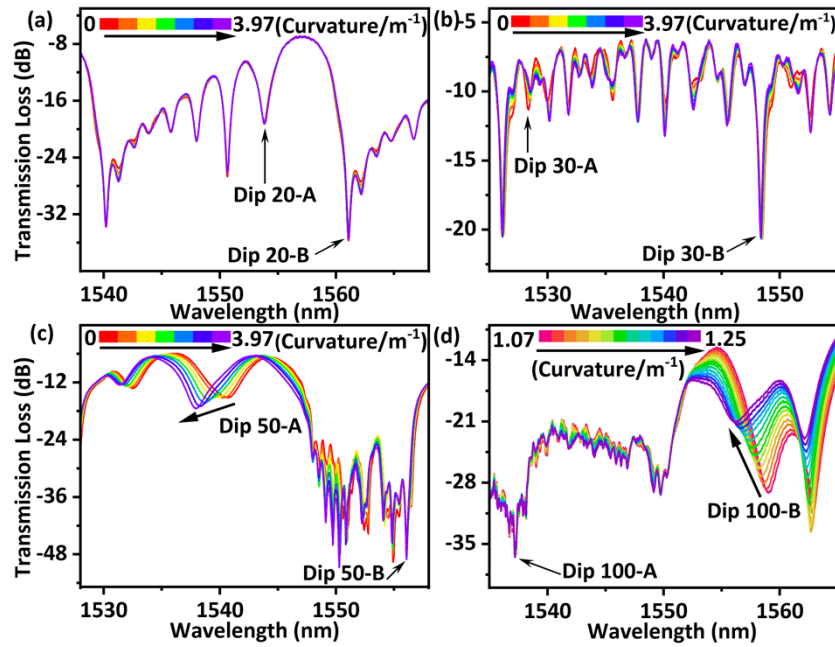


Fig. 9. FFT spectra of Fig. 7.

MMI, confirming that both ARROW and MMI guiding mechanisms are excited in large air core CFs (air core diameter  $> 30 \mu\text{m}$ ). It is noted that the MMI guiding mechanism could exist in a smaller air core diameter CF as demonstrated in the simulation shown in Fig. 4, but in practice the MMI dips are not excited due to high loss.

The wavelength shifts of dips 20-A, B, dips 30-A, B, dips 50-A, B and dips 100-A, B with respect to curvature are plotted in Fig. 11. All dips have linear responses to curvature changes in the measurement range and their corresponding sensitivities are summarized in Table 1. It can be seen that a higher curvature sensitivity is achieved in an CF with a larger air core diameter. Dip 100-B shows the highest curvature sensitivity of  $-16.15 \text{ nm/m}^{-1}$ , which is over two orders of magnitude higher than that of dip 100-A, and nearly 20 times higher than that of dip 50-A. Table 2 shows the comparison of curvature sensitivities of different fiber sensor structures [18,30–35,41–45]. Furthermore, the intensity variation of dip 100-A and B are shown in dip strength change in Fig. 12, where the sensitivities are  $-2.84 \text{ dB/m}^{-1}$  and  $48.84 \text{ dB/m}^{-1}$ . The dip intensity variations were observed due to the introduced bending loss [46]. The proposed sensor shows better curvature sensitivity than many modified SMF-multimode fiber-SMF structure sensors [19,26,38,47]. It can be seen that an SCS structure offers competitive sensitivities combined with a simple fabrication technique. In addition, ARROW dips could be used for temperature calibration during curvature measurement [18].



**Fig. 10.** Measured spectral responses to curvature for the sensor samples (a) CF-20-3, (b) CF-30-4, (c) CF-50-30 and (d) CF-100-110.

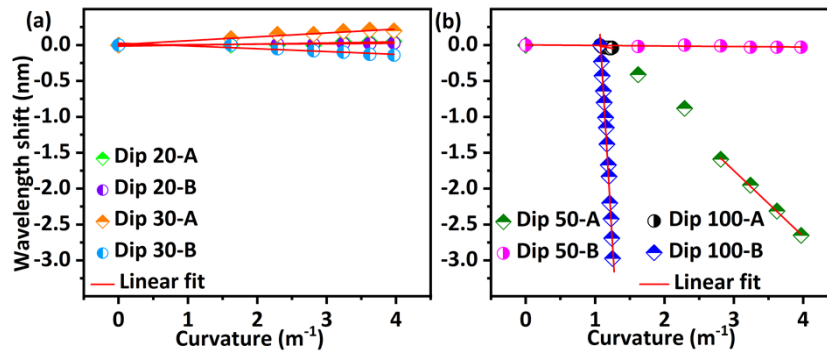


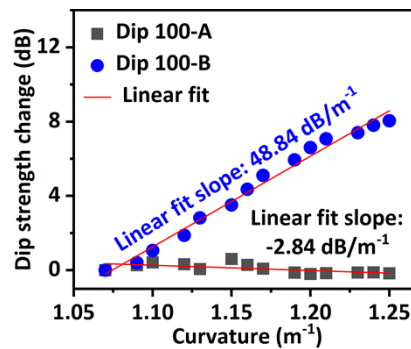
**Fig. 11.** Wavelength shifts with curvature changes for selected dipoles of different types of CF and their corresponding linear fits.

**Table 1. Selected dipoles and their sensitivities to curvature**

Dips	Central wavelength before bending (nm)	Sensitivity (nm/m <sup>-1</sup> )
CF-20-A	1553.81	0.01487
CF-20-B	1561.07	0.00654
CF-30-A	1528.35	0.05379
CF-30-B	1548.48	-0.0392
CF-50-A	1540.62	-0.91562
CF-50-B	1556.11	-0.0076
CF-100-A	1537.22	-0.14879
CF-100-B	1559.04	-16.15456

**Table 2. Comparison of the curvature sensitivities of SCS structures and other fiber structures**

Sensor	Sensitivity	Measurement range	Ref.
SMF-CF-75 (core diameter of 75 $\mu\text{m}$ )-SMF	0.2345 nm/m <sup>-1</sup>	[3.210 m <sup>-1</sup> , 5.560 m <sup>-1</sup> ]	30
SMF-ARHCF-SMF	0.7 nm/m <sup>-1</sup>	[0.6 m <sup>-1</sup> , 1.6 m <sup>-1</sup> ]	31
SMF-MMF (twisted)-SMF	-2.42 nm/m <sup>-1</sup>	[0 m <sup>-1</sup> , 1.7390 m <sup>-1</sup> ]	32
SMF inscribed with in-line MZI and FBG	2.491 nm/m <sup>-1</sup> (180°)	[0 m <sup>-1</sup> , 10 m <sup>-1</sup> ]	33
SMF with cascaded fiber interferometer	4.362 nm/m <sup>-1</sup>	[0 m <sup>-1</sup> , 1.134 m <sup>-1</sup> ]	34
Multicores fiber with Long period gratings	-4.85 nm/m <sup>-1</sup>	[0 m <sup>-1</sup> , 1.77 m <sup>-1</sup> ]	35
SMF-no core fiber-SMF (twisted)	16.28 nm/m <sup>-1</sup>	[0.96 m <sup>-1</sup> , 1.92 m <sup>-1</sup> ]	41
Two-mode fiber (with Long period grating)	-23.67 nm/m <sup>-1</sup>	[1.137 m <sup>-1</sup> , 4.684 m <sup>-1</sup> ]	42
Photonic bandgap fiber	24.3 nm/m <sup>-1</sup>	[0 m <sup>-1</sup> , 1.75 m <sup>-1</sup> ]	43
Four-core Sapphire-derived fiber	-24.526 nm/m <sup>-1</sup>	[-10 m <sup>-1</sup> , 5 m <sup>-1</sup> ]	44
Seven-core fiber (twisted)	-25.16 nm/m <sup>-1</sup>	[0.5201 m <sup>-1</sup> , 1.0071 m <sup>-1</sup> ]	45
SMF-CF-50-SMF	-2.02 nm/m <sup>-1</sup>	[7.04 m <sup>-1</sup> , 11.87 m <sup>-1</sup> ]	18
SMF-CF-50-SMF	<b>0.91 nm/m<sup>-1</sup></b>	<b>[2.81 m<sup>-1</sup>, 3.91 m<sup>-1</sup>]</b>	<b>This work</b>
SMF-CF-100-SMF	<b>-16.15 nm/m<sup>-1</sup></b>	<b>[1.07 m<sup>-1</sup>, 1.25 m<sup>-1</sup>]</b>	<b>This work</b>

**Fig. 12.** The dip strength changes of dip 100-A and B at different curvatures and Linear fits.

#### 4.3. Bidirectional liquid level measurement using the cascaded capillary fiber structure

At the present time, most of the CF-based cascade structure were employed to construct FPIs [48] and MZIs [49], few researches were conducted on cascaded CFs structures based on ARROW guiding mechanism [15]. Since the resonant wavelengths of a CF structure is dependent on the thickness of the silica cladding, simultaneous measurement of multiple parameters using multi-point sensors could be achieved by incorporating different types of CFs in a single sensor system [15]. In our previous works [23–24], we reported a high sensitivity liquid level sensor based on a single CF, which was not capable of detecting the liquid flow direction. Here we demonstrate a bi-direction liquid level measurement by employing two cascaded CFs with different air core diameters. In general, CFs with a relatively small air core diameter ( $\leq 30 \mu\text{m}$ ) are preferable for the fabrication of an SCCS structure for the bi-direction liquid level measurement, since they allow for the achievement of a higher sensitivity and also for exclusion of the influence of MMI dips. Specifically in this work, two sections of a CF-20 and a CF-30 were cascaded fusion spliced between two SMFs to construct a SMF-CF-30-CF-20-SMF (SCCS) structure.

Figure 13 illustrates the schematic diagram of the proposed SCCS structure and the experimental setup for liquid level measurement. The fiber sensor was placed in a transparent soft tube (inner diameter~3 mm), and its two SMF ends were fixed on two glass slides. Liquid (stilled water) was pumped into the soft tube by a peristaltic pump (Baoding Qili Precision Pump Cooperation, BT100-02) which can control both the liquid flow direction and speed. All liquid level variations were measured with the help of an optical microscope as a reference. Light from a SC was launched into the SCCS structure and the transmitted light was collected by an OSA.

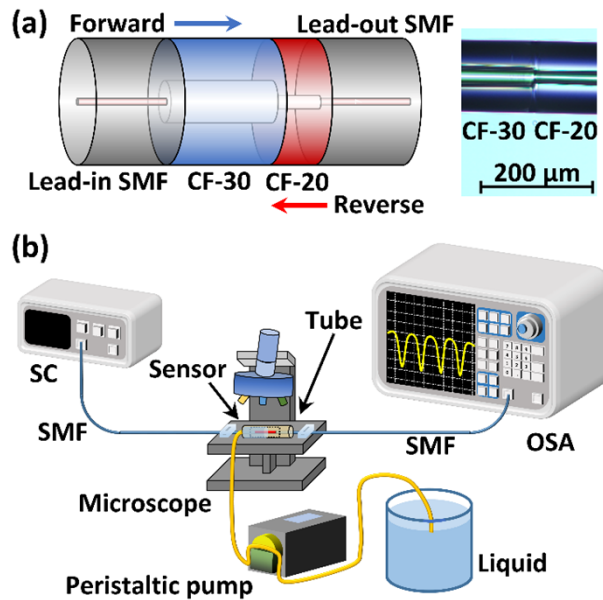


**Fig. 13.** (a) Schematic diagram of the SMF-CF-30-CF-20-SMF structure and a microscope image of showing splicing joint between CF-30 and CF-20. (b) Schematic diagram of the experimental setup for bi-direction liquid level measurement.

In our previous work [23], we have demonstrated that the strength of the ARROW dip is highly dependent on the reflection coefficient at the interface between the silica cladding and the outer environment, and a tiny change in the reflection coefficient could result in a significant change in the ARROW dip strength. The resonant condition for a radial FP etalon formed in the silica cladding is modulated by reducing the RI contrast between the silica cladding and external medium when the surrounding air is replaced with water, hence a SCS structure can be used as a high sensitivity liquid level sensor. An SCCS structure has two types of periodic transmission dips at different resonant wavelengths, and hence the two CFs can act as two independent liquid level sensors, which when cascaded allow for measurement of both liquid flow direction and liquid levels.

To balance the trade-off between the sensitivity and transmission loss, a 4.5 mm length of CF-30 and a 2 mm length of CF-20 were chosen for the fabrication of a SCCS structure. Figure 14 shows the transmission spectra of the proposed SCCS structure at different water levels where ARROW dips excited in the CF-20 and CF-30 can be easily identified from the central wavelengths of the dips. Then the SCCS structure was used for bi-directional liquid level measurement. The measured spectral responses with liquid level variations are shown in Fig. 14 and the corresponding dip strength changes are summarized in Fig. 15. As can be seen from the figure, when the CF-30 was gradually covered with water while the CF-20 was exposed to air, the strength of Dip-30 decreased while there was almost no change in the Dip-20 strength.

Similarly, when the CF-20 was gradually covered with water while CF-30 was exposed to air, the strength of Dip-20 decreased while the strength of Dip-30 almost didn't change. Therefore, both liquid level and liquid flow direction can be identified by simultaneously tracing the dip strength changes of Dip-20 and Dip-30. The maximum liquid level sensitivity of Dip-20 and Dip-30 are 0.014 dB/ $\mu\text{m}$  and 0.005 dB/ $\mu\text{m}$ , respectively. It is noted that the proposed fiber sensor can determine the liquid levels and liquid flow directions as long as the sensor head is not completely covered by the liquid because the dip strength of Dip-20 and Dip-30 are different at any point along the sensor head.

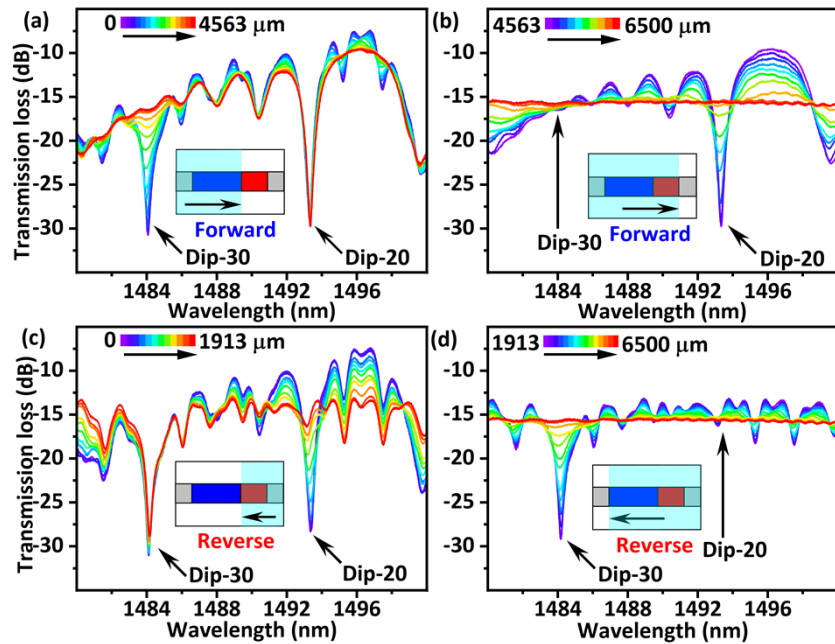


**Fig. 14.** Measured spectral responses under various liquid levels: (a), (b) water flows forward from CF-30 to CF-20. (c), (d) Water flows in the reverse direction from CF-20 to CF-30.

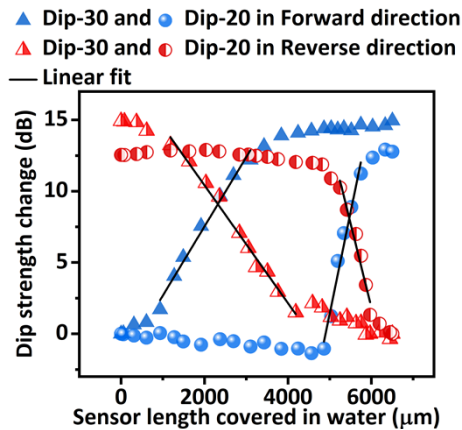


**Fig. 15.** Dip strength changes of Dip-30 and Dip-20 at different water levels and directions.



## 5. Conclusion

In conclusion, the light guiding mechanisms in an SCS structure with a large air core diameter (20  $\mu\text{m}$  to 100  $\mu\text{m}$ ) and long CF length ( $> 1$  mm) have been studied and discussed. Both BPM and FEM methods were used to study the light transmission properties and mode field properties of the SCS structure. It is found that both MMI and ARROW mechanisms are excited in transmission, which is verified by the experimental results. In bending experiments, it is found that the SCS sensor with a larger core diameter of CF has a higher sensitivity, and the highest curvature sensitivity of  $-16.15 \text{ nm/m}^{-1}$  was achieved for the sensor based on CF-100, which is nearly 20 times higher than that of the CF-50. In addition, an SCCS structure is proposed by cascaded splicing two sections of CF-20 and CF-30 between two SMFs. Two types of ARROW dips (Dip-20 and Dip-30) are simultaneously excited in the transmission spectrum of the SCCS structure which can act as a high sensitivity bi-direction liquid level sensor by tracing the dip strength changes of both ARROW dips (Dip-20 and Dip-30).

**Funding.** National Natural Science Foundation of China (11874332, 62105217); Basic and Applied Basic Research Foundation of Guangdong Province (2019A1515110320); Shenzhen Fundamental Research Program (JCYJ20190808140805488, JCYJ20190808173401660, JCYJ20190808173619062); National Key Scientific Instrument and Equipment Development Projects of China (61727816).

**Disclosures.** The authors declare no conflicts of interest.

**Data availability.** Data underlying the results presented in this paper are not publicly available at this time but may be obtained from the authors upon reasonable request.

## References

1. N. González-Baquedano, I. Torres-Gómez, N. Arzate, A. Ferrando, and D. E. Ceballos-Herrera, "Pulse quality analysis on soliton pulse compression and soliton self-frequency shift in a hollow-core photonic bandgap fiber," *Opt. Express* **21**(7), 9132–9143 (2013).
2. D. Schade, F. Köttig, J. R. Koehler, M. H. Frosz, P. S. J. Russell, and F. Tani, "Scaling rules for high quality soliton self-compression in hollow-core fibers," *Opt. Express* **29**(12), 19147–19158 (2021).
3. J. R. Hayes, S. R. Sandoghchi, T. D. Bradley, Z. Liu, R. Slavík, M. A. Gouveia, N. V. Wheeler, G. Jasion, Y. Chen, E. N. Fokoua, M. N. Petrovich, D. J. Richardson, and F. Poletti, "Antiresonant Hollow Core Fiber With an Octave Spanning Bandwidth for Short Haul Data Communications," *J. Lightwave Technol.* **35**(3), 437–442 (2017).
4. C. Lin, C. Liao, Y. Zhang, L. Xu, Y. Wang, C. Fu, K. Yang, J. Wang, J. He, and Y. Wang, "Optofluidic gutter oil discrimination based on a hybrid-waveguide coupler in fibre," *Lab Chip* **18**(4), 595–600 (2018).
5. L. Li and L. Xiao, "Plasmonic Nodeless Hollow-Core Photonic Crystal Fibers for In-Fiber Polarizers," *J. Lightwave Technol.* **37**(20), 5199–5211 (2019).
6. S. Meiselman and G. A. Cranch, "Optical phase response to temperature in a hollow-core photonic crystal fiber," *Opt. Express* **25**(22), 27581–27594 (2017).
7. M. Hou, Y. Wang, S. Liu, J. Guo, Z. Li, and P. Lu, "Sensitivity-Enhanced Pressure Sensor With Hollow-Core Photonic Crystal Fiber," *J. Lightwave Technol.* **32**(23), 4035–4039 (2014).
8. J. Yang, M. Yang, C. Y. Guan, J. H. Shi, Z. Zhu, P. Li, P. F. Wang, J. Yang, and L. B. Yuan, "In-fiber Mach-Zehnder interferometer with piecewise interference spectrum based on hole-assisted dual-core fiber for refractive index sensing," *Opt. Express* **26**(15), 19091–19099 (2018).
9. J. Zhang, C. Guan, Y. Jin, P. Ye, T. Cheng, J. Yang, P. Tian, Z. Zhu, J. Shi, J. Yang, and L. Yuan, "Temperature and Refractive Index-Independent Mode Converter Based on Tapered Hole-Assisted Dual-Core Fiber," *J. Lightwave Technol.* **39**(8), 2522–2527 (2021).
10. W. Ni, P. Lu, J. Zhang, C. Yang, X. Fu, Y. Sun, H. Liao, and D. Liu, "Single hole twin eccentric core fiber sensor based on anti-resonant effect combined with inline Mach-Zehnder interferometer," *Opt. Express* **25**(11), 12372–12380 (2017).
11. W. Ni, P. Lu, X. Fu, H. Sun, P. P. Shum, H. Liao, X. Jiang, D. Liu, C. Yang, J. Zhang, and Z. Lian, "Simultaneous implementation of enhanced resolution and large dynamic range for fiber temperature sensing based on different optical transmission mechanisms," *Opt. Express* **26**(14), 18341–18350 (2018).
12. D. Liu, W. Li, Q. Wu, H. Zhao, F. Ling, K. Tian, C. Shen, F. Wei, W. Han, G. Farrell, Y. Semenova, and P. Wang, "Negative Curvature Hollow Core Fiber Based All-Fiber Interferometer and Its Sensing Applications to Temperature and Strain," *Sensors* **20**(17), 4763 (2020).
13. R. Gao, D. Lu, J. Cheng, Y. Jiang, L. Jiang, and Z. Qi, "Optical Displacement Sensor in a Capillary Covered Hollow Core Fiber Based on Anti-Resonant Reflecting Guidance," *IEEE J. Sel. Top. Quantum Electron.* **23**(2), 193–198 (2017).
14. S. Liu, Y. Ji, L. Cui, W. Sun, J. Yang, and H. Li, "Humidity-insensitive temperature sensor based on a quartz capillary anti-resonant reflection optical waveguide," *Opt. Express* **25**(16), 18929–18939 (2017).

15. N. Cai, L. Xia, and Y. Wu, "Multiplexing of anti-resonant reflecting optical waveguides for temperature sensing based on quartz capillary," *Opt. Express* **26**(25), 33501–33509 (2018).
16. D. Liu, Q. Wu, C. Mei, J. Yuan, X. Xin, A. K. Mallik, F. Wei, W. Han, R. Kumar, C. Yu, S. Wan, X. He, B. Liu, G. Peng, Y. Semenova, and G. Farrell, "Hollow Core Fiber Based Interferometer for High-Temperature (1000 °C) Measurement," *J. Lightwave Technol.* **36**(9), 1583–1590 (2018).
17. R. Gao, D. Lu, J. Cheng, Y. Jiang, L. Jiang, and Z. Qi, "Humidity sensor based on power leakage at resonance wavelengths of a hollow core fiber coated with reduced graphene oxide," *Sens. Actuators, B* **222**, 618–624 (2016).
18. S. Wang, C. Shan, J. Jiang, K. Liu, X. Zhang, Q. Han, J. Lei, H. Xiao, and T. Liu, "Temperature-insensitive curvature sensor based on anti-resonant reflection guidance and Mach–Zehnder interferometer hybrid mechanism," *Appl. Phys. Express* **12**(10), 106503 (2019).
19. S. Wang, S. Wang, S. Zhang, M. Feng, S. Wu, R. Jin, L. Zhang, and P. Lu, "An inline fiber curvature sensor based on anti-resonant reflecting guidance in silica tube," *Opt. Laser Technol.* **111**, 407–410 (2019).
20. D. Liu, R. Kumar, F. Wei, W. Han, A. K. Mallik, J. Yuan, C. Yu, Z. Kang, F. Li, Z. Liu, H. Tam, G. Farrell, Y. Semenova, and Q. Wu, "Highly Sensitive Twist Sensor Based on Partially Silver Coated Hollow Core Fiber Structure," *J. Lightwave Technol.* **36**(17), 3672–3677 (2018).
21. D. Liu, W. Li, Q. Wu, F. Ling, K. Tian, C. Shen, F. Wei, G. Farrell, Y. Semenova, and P. Wang, "Strain-, curvature- and twist-independent temperature sensor based on a small air core hollow core fiber structure," *Opt. Express* **29**(17), 26353–26365 (2021).
22. F. Qi, L. Hu, X. Dong, Y. Xin, C. Zhao, S. Jin, and J. C. C. Chan, "A Hollow Core Fiber-Based Intermodal Interferometer for Measurement of Strain and Temperature," *IEEE Sens. J.* **13**(9), 3468–3471 (2013).
23. D. Liu, F. Ling, R. Kumar, A. K. Mallik, K. Tian, C. Shen, G. Farrell, Y. Semenova, Q. Wu, and P. Wang, "Sub-micrometer resolution liquid level sensor based on a hollow core fiber structure," *Opt. Lett.* **44**(8), 2125–2128 (2019).
24. D. Liu, W. Li, Q. Wu, H. Zhao, F. Ling, K. Tian, C. Shen, W. Han, F. Wei, G. Farrell, Y. Semenova, and P. Wang, "High sensitivity liquid level sensor for microfluidic applications using a hollow core fiber structure," *Sens. Actuators, A* **332**, 113134 (2021).
25. H. Gao, Y. Jiang, L. Zhang, Y. Cui, Y. Jiang, J. Jia, and L. Jiang, "Antiresonant mechanism based self-temperature-calibrated fiber optic Fabry–Perot gas pressure sensors," *Opt. Express* **27**(16), 22181–22189 (2019).
26. H. Cheng, S. Wu, Q. Wang, S. Wang, and P. Lu, "In-Line Hybrid Fiber Sensor for Curvature and Temperature Measurement," *IEEE Photonics J.* **11**(6), 1–11 (2019).
27. T. Nan, B. Liu, Y. Wu, Y. Mao, J. Wang, L. Zhao, T. Sun, J. Wang, and Y. Han, "Three-parameter measurement optical fiber sensor based on a hybrid structure," *Appl. Opt.* **59**(27), 8190–8195 (2020).
28. W. Sun, X. Zhang, Y. Yu, L. Yang, F. Hou, Y. Yang, and T. Wang, "Comparative Study on Transmission Mechanisms in a SMF-Capillary-SMF Structure," *J. Lightwave Technol.* **38**(15), 1 (2020).
29. Y. Yu, X. Zhang, K. Wang, Z. Wang, H. Sun, Y. Yang, C. Deng, Y. Huang, and T. Wang, "Coexistence of transmission mechanisms for independent multi-parameter sensing in a silica capillary-based cascaded structure," *Opt. Express* **29**(17), 27938–27950 (2021).
30. B. Qi, B. Su, F. Zhang, L. Zhong, O. Xu, and Y. Qin, "A Compact Fiber Cascaded Structure Incorporating Hollow Core Fiber With Large Inner Diameter for Simultaneous Measurement of Curvature and Temperature," *IEEE Photonics J.* **14**(1), 1–8 (2022).
31. C. Goel, J. Zang, M. Parrot, and S. Yoo, "Temperature-Insensitive Mechanical Sensor Using Multi-Modal Behavior of Antiresonant Hollow-Core Fibers," *J. Lightwave Technol.* **39**(12), 3998–4005 (2021).
32. K. Tian, Y. Xin, W. Yang, T. Geng, J. Ren, Y. Fan, G. Farrell, E. Lewis, and P. Wang, "A Curvature Sensor Based on Twisted Single-Mode–Multimode–Single-Mode Hybrid Optical Fiber Structure," *J. Lightwave Technol.* **35**(9), 1725–1731 (2017).
33. Z. Rong, X. Shu, and Z. Xu, "Compact Fiber Curvature and Temperature Sensor Inscribed by Femtosecond Laser Through the Coating," *J. Lightwave Technol.* **39**(12), 3981–3990 (2021).
34. S. Dong, B. Dong, C. Yu, and Y. Guo, "High Sensitivity Optical Fiber Curvature Sensor Based on Cascaded Fiber Interferometer," *J. Lightwave Technol.* **36**(4), 1125–1130 (2018).
35. D. Barrera, J. Madrigal, and S. Sales, "Long Period Gratings in Multicore Optical Fibers for Directional Curvature Sensor Implementation," *J. Lightwave Technol.* **36**(4), 1063–1068 (2018).
36. K. Zhang, H. Pan, H. Bai, M. Yan, J. Wang, C. Deng, and T. Wang, "Transition of Fabry–Perot and antiresonant mechanisms via a SMF-capillary-SMF structure," *Opt. Lett.* **43**(10), 2268–2271 (2018).
37. Y. Jung, S. Lee, B. H. Lee, and K. Oh, "Ultra-compact in-line broadband Mach-Zehnder interferometer using a composite leaky hollow-optical-fiber waveguide," *Opt. Lett.* **33**(24), 2934–2936 (2008).
38. S. Marrujo-García, I. Hernández-Romano, M. Torres-Cisneros, D. A. May-Arrijoja, V. P. Minkovich, and D. Monzón-Hernández, "Temperature-Independent Curvature Sensor Based on In-Fiber Mach–Zehnder Interferometer Using Hollow-Core Fiber," *J. Lightwave Technol.* **38**(15), 1 (2020).
39. Y. Wang, D. Richardson, G. Brambilla, X. Feng, M. Petrovich, M. Ding, and Z. Song, "Intensity measurement bend sensors based on periodically tapered soft glass fibers," *Opt. Lett.* **36**(4), 558–560 (2011).
40. R. Gao, Y. Jiang, and Y. Zhao, "Magnetic field sensor based on anti-resonant reflecting guidance in the magnetic gel-coated hollow core fiber," *Opt. Lett.* **39**(21), 6293–6296 (2014).

41. W. Zhuang, H. Niu, M. Dong, and L. Zhu, "A curvature sensor based on single mode-no-core-twisted single mode fiber structure," *Opt. Fiber Technol.* **48**, 225–228 (2019).
42. T. Liu, A. Chen, M. Sang, J. Zhang, S. Wang, J. Jiang, and J. Dong, "High sensitivity curvature sensor based on the long period fiber grating inscribed in the two-mode fiber," *Appl. Opt.* **60**(30), 9280–9286 (2021).
43. X. Hu, J. Peng, L. Yang, J. Li, H. Li, and N. Dai, "Design and fabrication of a heterostructured cladding solid-core photonic bandgap fiber for construction of Mach-Zehnder interferometer and high sensitive curvature sensor," *Opt. Express* **26**(6), 7005–7012 (2018).
44. Z. Wang, L. Zhang, Z. Ma, Z. Chen, T. Wang, and F. Pang, "High-Sensitivity Bending Sensor Based on Supermode Interference in Coupled Four-Core Sapphire-Derived Fiber," *J. Lightwave Technol.* **39**(12), 3932–3940 (2021).
45. W. Chen, Z. Chen, Y. Qiu, L. Kong, H. Lin, C. Jia, H. Chen, and H. Li, "Highly sensitive optical fiber curvature sensor based on a seven-core fiber with a twisted structure," *Appl. Opt.* **58**(32), 8776–8784 (2019).
46. L. A. Herrera-Piada, I. Hernández-Romano, D. A. May-Arrijoja, V. P. Minkovich, and M. Torres-Cisneros, "Sensitivity Enhancement of Curvature Fiber Sensor Based on Polymer-Coated Capillary Hollow-Core Fiber," *Sensors* **20**(13), 3763 (2020).
47. Y. Zhang, A. Zhou, B. Qin, Q. Xu, Z. Liu, J. Yang, and L. Yuan, "Simultaneous Measurement of Temperature and Curvature Based on Hollow Annular Core Fiber," *IEEE Photonics Technol. Lett.* **26**(11), 1128–1131 (2014).
48. Y. Liu, Y. Wang, D. Yang, J. Wu, T. Zhang, D. Yu, Z. Jia, and H. Fu, "Hollow-Core Fiber-Based All-Fiber FPI Sensor for Simultaneous Measurement of Air Pressure and Temperature," *IEEE Sens. J.* **19**(23), 11236–11241 (2019).
49. M. Hou, J. He, X. Xu, Z. Li, Z. Zhang, K. Guo, S. Ju, and Y. Wang, "Antiresonant Reflecting Guidance and Mach-Zehnder Interference in Cascaded Hollow-Core Fibers for Multi-Parameter Sensing," *Sensors* **18**(12), 4140 (2018).